Analysis of the transition from flat to slanted fatigue crack growth in thin metallic sheets

Jean-Baptiste Esnault [1,2], Véronique Doquet [1,*], Patrick Massin[2]

[1] : Laboratoire de Mécanique des Solides, CNRS, Ecole Polytechnique, Palaiseau France

[2] LaMSid, EDF – CNRS - CEA, Clamart, France

*corresponding author: doquet@lms.polytechnique.fr

Abstract Fatigue crack growth in thin sheets of 7075 T651 aluminium alloy and S355 steel were characterized in 3D, using crack front markings and topographic reconstructions of fracture surfaces. Tests performed in air or in salt water produced different crack paths for similar mechanical conditions, shear lips being reduced by the corrosive environment, in the aluminium alloy as well as in steel. Before the onset of shear lips development, tunnelling crack fronts were observed, due to the difference in closure effects at mid-thickness and near the free surfaces. Tunnelling was progressively reduced and cancelled as slanted crack growth developed, even though ΔK_I was reduced locally by crack twisting. This indicates a significant contribution of shear modes to the crack driving force, even though mode I striations are present in the slanted zones. Elastic three-dimensional X-FEM computations were performed to analyse the observed crack growth kinetics, based on ΔK_I, ΔK_{II} and ΔK_{III}. The crack growth rates correlated much better to $\Delta K_{eq} = \sqrt{\Delta K_I^2 + \Delta K_{II}^2 + \frac{\Delta K_{III}^2}{(1-\nu)}}$ than to ΔK_I. Elastic-plastic finite element simulations and the local application of a fatigue criterion with an amplitude-dependent critical plane were found to capture qualitatively the transition in fracture mode.

Keywords fatigue crack, shear lips, thin sheet, mixed-mode, X-FEM, slanted crack

1. Introduction

Fatigue crack growth normal to the tensile axis becomes unstable in thin metallic sheets, above a material, environment and frequency-dependent amplitude, even though, in many cases, small scale yielding conditions still prevail. Shear lips development has been investigated mainly in aluminium alloys by Schijve and coworkers [1-2] Zuidema et al. [3-4] or Shanyavsky and Koronov [5], while a few studies were devoted to steel [6] or titanium alloys [7]. Walker et al [7] first reported an influence of environment on shear lips development in titanium alloys. The corrosive environment appeared to postpone crack twisting in Ti-8Al-1Mo-1V, while no systematic effect was found in Ti-6Al-AV. Vogelesang and Schijve [2] observed complete crack twisting in 7075 T651 aluminium alloy for a lower apparent ΔK_I in vacuum than in air and for a higher apparent ΔK_I in 3,5%NaCl solution. Horibe et al [6] reported a similar effect of salt water in low strength steel, but a less pronounced effect of environment for high strength steel. Shanyavsky and Koronov [5] measured the shear lips width in thin aluminium alloy cruciform specimens cyclically loaded in two orthogonal directions and reported that a positive biaxiality ratio reduced the shear lips, while a negative ratio increased it. They also observed a reduction in shear lips width when the R ratio increased. This observation conflicts with the conclusion of Zuidema et al. [3-4] that the

"steady-state" shear lips is a linearly increasing function of the effective ΔK, which usually increases with R.

The analyses of experimental data in the literature are essentially two-dimensional. Slanted crack growth kinetic data is analysed as if it was mode I and as if the growth rate and driving force were uniform along the front. Based on "constant ΔK_I tests", empirical relations between the steady-state shear lips width, the loading frequency and the "effective ΔK_I" were derived for aluminium alloys [3-4]. This parameter will be denoted below by "apparent ΔK_I", since it is computed in 2D for a normal crack of same length as that observed on the free surface, with an empirical correction for closure effects deduced from the R ratio. The meaning of "constant ΔK_I tests" is also questionable in view of the large gradient in K_I, K_{II} and K_{III} along the front of a partially or completely slanted crack and of the reduction in ΔK_I associated with crack twisting.

In an effort toward 3D analysis, Pook [8] performed finite element computations of the stress intensity factors along the front of a fully slanted crack in specimens of different thickness. He found that K_I was 0.51 to 0.71 smaller than its apparent value (computed in 2D for a normal crack of same length). He also found that K_{III} had the same order of magnitude as K_I, while K_{II} raised near the free surfaces with a skew-symmetric profile. Bakker [9] performed 3D computations of stress intensity factors for fully or partially slanted crack. However, as in the case studied by Pook, a straight crack front was considered, while tunnelling probably plays a role in crack twisting in fatigue.

The present work re-examines the problem from a 3D perspective, in order to determine what mechanical parameters control the onset of crack deviation and the kinetics of slanted crack growth. Since environment seemed to influence shear lips development, a 3D experimental characterization of the crack paths and kinetics was performed, both in air and in salt water and the crack paths were compared. A 3D numerical analysis of the crack growth rates was done, based on linear elastic fracture mechanics, taking mode-mixity into account. Elastic-plastic computations of stress and strain fields ahead of the crack front were used to rationalize the observed crack paths. A method to predict the onset of crack twisting and the twist angles was proposed.

2. Experimental procedures

Fatigue crack growth tests were performed with a frequency of 5Hz and R=0.1 on 6mm-thick, 100mm-wide, 300mm-high Center-Cracked Panels (CCP) specimens. Two material were investigated: 7075-T651 aluminium alloy ($\sigma_{0,2}$= 376MPa, σ_u= 537MPa, E= 75 GPa) and S355 low-alloy steel ($\sigma_{0,2}$= 349MPa, σ_u= 510MPa, E= 205 GPa). Both sides of the specimens were polished to allow crack propagation monitoring with an optical microscope, at a magnification of one hundred. The tests were performed in air or in a transparent reservoir filled with 3,5g/l NaCl solution, under different loading amplitudes indicated in Table 1. Marker block loading sequences with and increased K_{min} but the same K_{max} were periodically applied, so that the R ratio became temporary 0.7, until approximately 100 μm propagation was achieved, in order to mark the position of the crack front and be able to derive the mean crack growth rate between consecutive markings, for any point along the front. Ten to twelve marker blocks were applied at 20Hz. To characterize crack front tunnelling, the difference in crack length between the mid-thickness and the average length on free surfaces was measured and denoted by Δa.

Table 1: Test conditions

Material	7075 T651			S355 steel	
Test n°	CCP7a	CCP7Na	CCP5a	CCP2a	CCP2Na
Environment	air	NaCl	air	air	NaCl
Range of apparent ΔK_I (Mpa$\sqrt{m}$)	7-18	7-18	9-20	18-35	18-35
Stress range (MPa)	34	34	40	100	100
Cycles for crack initiation	30000	10000	15000	35000	27000
Cycles of crack growth until fracture	202440	110260	59000	157730	138730

Fracture surface topographies were reconstructed using a digital optical microscope. The results were obtained as (x, y, z) triplets, where x denotes the distance from the notch root, y, the position in depth, and z the height from the notch plane. Transverse height profiles, z(y) were derived. Polynomial expressions were fitted to these profiles and used to compute the local twist angle as arctang (dz/dy). The shear lips width, denoted by t_s, was deduced from these height profiles.

3. Experimental results

Salt water reduced the number of cycles for crack initiation by a factor of 3 in the aluminium alloy and 1.3 in steel. Crack growth was significantly accelerated in the aluminium alloy, but not in steel. Figure 1 shows examples of crack transverse profiles, z(y), and twist angle profiles at different stages of crack growth.

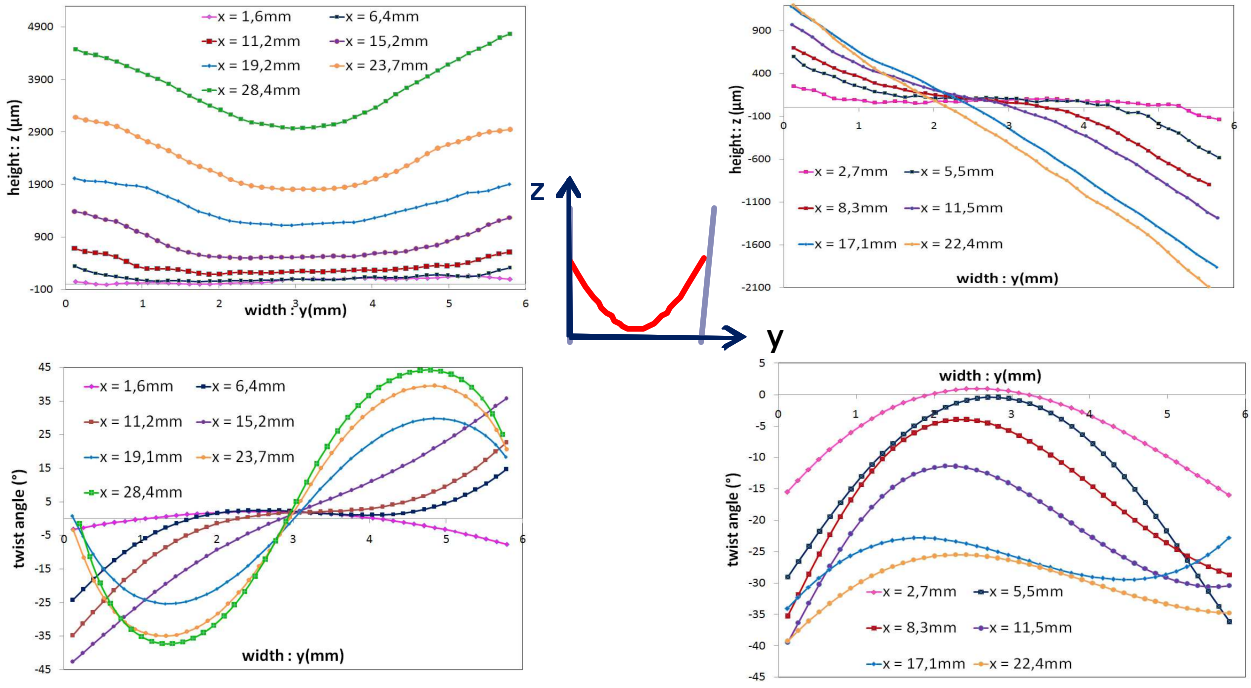

Fig 1: Topographic reconstructions of fracture surfaces. a) transverse profiles and b) twist angles for specimen CCP5a. c) transverse profiles and d) twist angles for specimen CCP2a.

The twist angle is neither uniform along the shear lip, nor constant as the crack grows. It is substantially less than 45°. In some cases, the peak value is not observed at the free surface but up to 1mm in depth. The evolutions of the shear lips width in air and NaCl solution under the same mechanical conditions are compared on Fig 2.

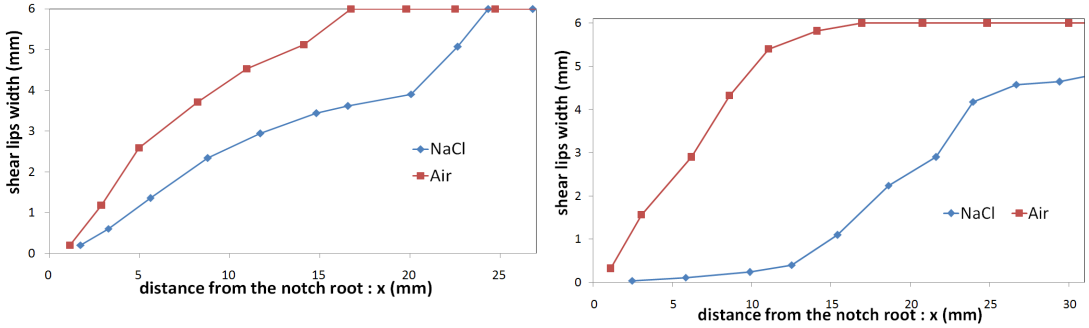

Fig 2: Evolution of shear lips width in air and NaCl solution under similar loading conditions
a) specimens CCP7a and CCP7Na and b) steel specimens CC2a and CCP2Na

Shear lips development was delayed and less complete in the NaCl solution, in agreement with some observations from the literature [2, 6]. The evolution of crack front tunnelling, Δa, is plotted on Fig 3.

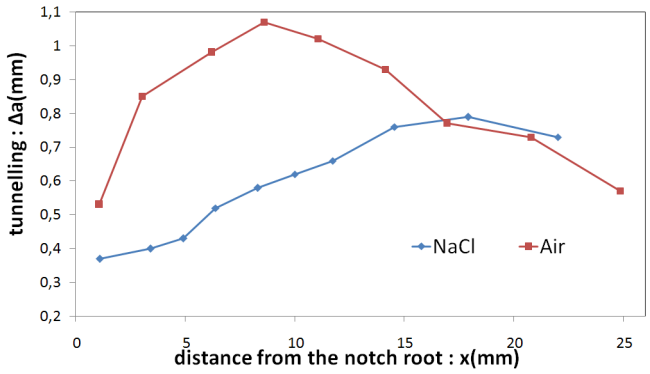

Fig 3: Evolution of crack front tunnelling, in steel specimens, in air or NaCl solution

In air, tunnelling was progressively reduced and cancelled by the development of shear lips, in spite of a drop in nominal ΔK_I in the slanted zones and of a probable local increase in closure effects, generally more important at low ΔK_I. Both factors should reduce the crack growth rate near the free surfaces and thus increase the convexity of the front. A reverse effect is observed. The reduction of tunnelling provides evidence for an effective contribution of shear modes to the crack driving force. However, fractographic observations revealed fatigue striations in normal zones as well as in slanted areas, where a few isolated rubbing marks were also observed near the side surfaces. Hence mode I still contributed to crack growth in the slanted zones and it would be incorrect to describe crack twisting as a transition from tension to shear-mode, as sometimes done in the literature.

4. Numerical study

The numerical study is constituted of two parts: 1) an elastic analysis in an extended finite element code (X-FEM, implemented in *Code_Aster* at EDF R&D, *www.**code-aster**.org/*) well fitted to

estimate the stress-intensity factors (SIFs) taking into account the real geometry of slanted cracks, but not suitable for the simulation of cyclic plasticity and 2) an elastic-plastic analysis carried out in the framework of the classical finite element method with Cast3M software (*www-**cast3m**.cea.fr/)*, therefore limited to flat tunnelling cracks. The stress-intensity factors issued from the X-FEM computations will be used to analyse the measured crack growth rates and to determine the parameter which best correlates the data. But the SIFs are considered useless for the prediction of crack paths, since none of the bifurcation criteria based on those parameters can predict that a fatigue crack loaded in mode I changes its path to grow in mixed-mode along a shear lip. In the present case, the crack paths are believed to be determined by the stress and strain fields just ahead of the crack front, which must be computed by elastic-plastic cyclic computations.

4.1 ***The X-FEM computation***

4.1. a General framework

The extended finite element method, introduced by Moes et al. [10], allows the simulation of complex crack shapes where the structural finite element mesh does not have to conform to the crack surface. The crack surface and its front are defined geometrically by two signed distance functions named “level sets”. In order to take into account the displacement jump due to the presence of the crack and the crack tip singularity the discretized displacement field is “enriched” with discontinuous shape functions. The displacement field is approximated as follows:

$$u(x) = \sum_{i \in I_0} N_i(x) u_i + \sum_{i \in I_H} N_i(x) H(x).a_i + \sum_{i \in I\gamma} N_i(x) \left(\sum_{k=1,4} \gamma_k(x).b_{i,k} \right) \quad (1)$$

In which H denotes the Heavyside function: $H(x) = \begin{cases} -1 \, if & x < 0 \\ +1 \, if & x > 0 \end{cases}$ (2)

I_0 is the set of the standard finite element nodes, I_H the set of nodes whose support is completely cut by the crack and I_γ the set of nodes whose support contains the crack front, a_i and $b_{i,k}$, the corresponding additional degrees of freedom. N_i are the standard finite element shape functions, u_i the nodal displacements and γ_k is the base of Westergaard’s solution representing the asymptotic displacement field at the crack tip of a semi-infinite crack in an infinite medium:

$$\gamma_k(x) = \left\{ \sqrt{r} \sin(\frac{\theta}{2}), \sqrt{r} \cos(\frac{\theta}{2}), \sqrt{r} \sin(\frac{\theta}{2}) \sin(\theta), \sqrt{r} \sin(\theta) \cos(\frac{\theta}{2}) \right\} \quad (3)$$

4.1. b Representation of the crack.

One of the ways to generate the level–sets used to represent the crack is to mesh both the crack surface and the crack front. This mesh is used only for the geometrical description of the crack and not for the resolution of the problem. An algorithm was thus developed to turn the measured topographic data, that is: a set of (x, y, z) triplets plus polynomial fits of crack front markings, into a mesh representative of the crack. The first step is to fit a polynomial interpolation to the cloud of points extracted from the topography, using the least square method, in 3D. Then a regular, flat grid of points is deformed, using both the equation of the crack surface z(x, y), and the polynomial fit of its front, x(y) (Fig. 4). This grid is then meshed with quadrangles and the linear elements of the

crack front are extracted.

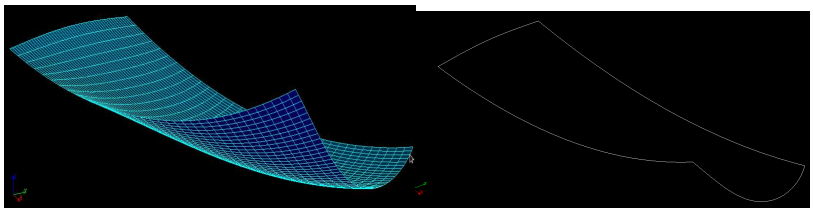

Fig 4: example of mesh of a crack surface used for level-sets computation

The G-θ method proposed by Destuynder et al. [11] was used to compute the SIFs. Due to corner point singularities, the values computed at surface points were not included in the analysis.

4.1. c The structural mesh.

Half of the CCP specimen was modelled with linear hexahedral (50µm*50µm*50µm) elements in a parallalepidal zone centered at the crack tip, linked to tetrahedral elements, via pyramidal elements, out of the process zone. The boundary conditions are indicated on Fig. 5.

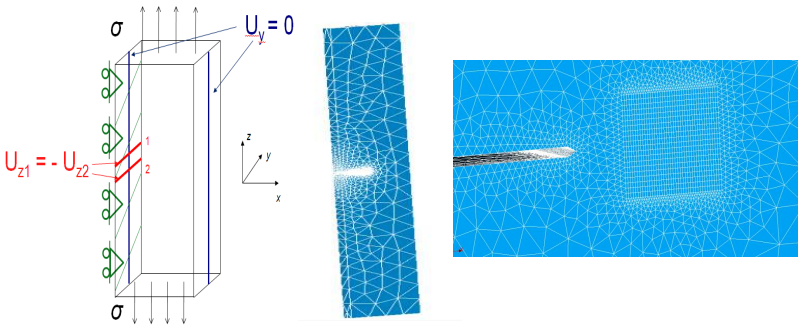

Fig 5: Boundary conditions and mesh of the CCP specimen in the X-FEM model

4.2. Elastic-plastic finite element analysis

This part focuses on the onset of crack twisting and thus considers flat, normal cracks, but takes tunnelling into account. Only a quarter of the CCP specimen was modelled, taking advantage of the symmetries. A 3D mesh with a straight crack front was first prepared, using linear elements, 30*30*150µm-wide near the crack front, which was then deformed, using the polynomial equation describing best the observed tunnelling front (Fig 7).

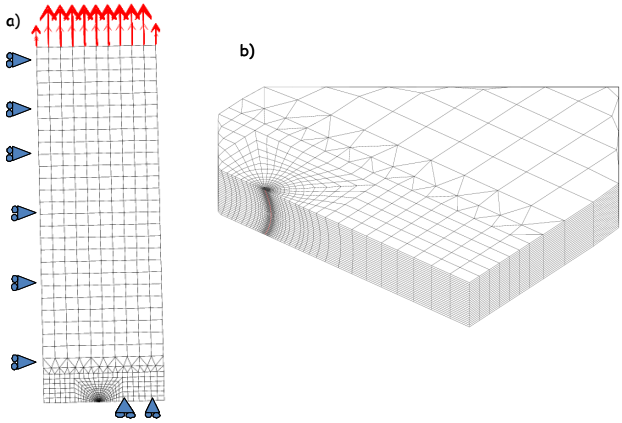

Figure 7: a) F.E. mesh of a quarter CCP specimen and boundary conditions, b) tunnelling crack front

Elastic-plastic constitutive equations with isotropic and non-linear kinematic hardening, identified from the stress-strain loops obtained from push-pull tests were used. Cyclic loading with R=0.1 was simulated. The stress and strain fields computed at maximum and minimum load were used for a local application, ahead of each node of the front, of a fatigue criterion derived from that identified by Zhao and Jiang from an extensive multiaxial fatigue database on 7075 T6 [12]. Their criterion successfully captured the transition in fracture mode observed in torsion as well as in push-pull or combined loading: when the loading range increases, fatigue damage changed from normal-stress-driven to shear-driven, yet with an assistance of an opening stress. Their damage function (DF) was thus:

$$DF = 2b\Delta\varepsilon_n \left\langle \sigma_{n\max} \right\rangle + \frac{1-b}{2}\Delta\tau\Delta\gamma \tag{4a}$$

$$b = \left\langle a_1 - a_2 \Delta\sigma_{eq} \right\rangle \tag{4b}$$

in which <x> denotes the positive part of x, a_1 and a_2 two fitted constants (0.862 and 0.00125), $\Delta\varepsilon_n$, $\Delta\gamma$, $\Delta\tau$, σ_{nmax}, respectively the normal strain, shear strain and stress range and peak opening stress, all computed along the critical plane. The latter is that for which the damage function, DF is maximum. As a consequence of Eq. 4b, the normal stress and strain play a major role at low stress range, but their influence decreases as the stress range increases, down to a transition stress range above which damage is merely driven by shear (b=0). In the present study, this criterion was slightly modified. The transition in fracture mode occurs in the low-cycle fatigue regime, where fatigue tests are usually strain-controlled, while the equivalent stress range evolves due to cyclic hardening. The value of $\Delta\sigma_{eq}$ which enters equation 4b was thus not clearly defined. The parameter b was thus considered to be more clearly related to the applied equivalent strain range, rather than to the stress range. Equation 4b was therefore turned into:

$$b = \left\langle 1 - \frac{2.\Delta\varepsilon_{eq}}{\Delta\varepsilon_{eq\,trans}} + \left(\frac{\Delta\varepsilon_{eq}}{\Delta\varepsilon_{eq\,trans}}\right)^2 \right\rangle \tag{5}$$

in which $\Delta\varepsilon_{eq,trans}$ corresponds to the equivalent strain range for which the transition from one fracture mode to the other is observed. A smoother evolution of b is predicted, compared to Eq. 4b. In addition, b tends toward 1 when the strain range vanishes, so that fracture is controlled merely by the normal stress and strain, which was not the case in the original criterion, for which the maximum value of b was 0.862. To apply the criterion ahead of each node of the crack front, $\Delta\varepsilon_{eq}$ was first averaged over a 90μm-long segment parallel to the x axis, comprising three elements. The local value of b was then computed using Eq. 5 with $\Delta\varepsilon_{eq,trans}$=0.92% for the aluminium alloy and 0.45% for steel. For each node, the damage function was computed, using the local value of b, along all potential twisted planes, for a twist angle θ ranging from 0 to 45°. The value of θ corresponding to the maximum of DF was considered as the local direction of crack extension. Here again stresses and strains were averaged over a distance of 90μm. This arbitrary distance, which influences the predicted crack paths should be considered as an adjustable parameter.

5. Numerical analysis of the experimental results

5.1. Computed SIFs and analysis of crack growth rates

Figure 8 shows the computed K_I, K_{II} and K_{III} computed at peak load along the 7th crack fronts in specimens CCP5a and CCP2a.

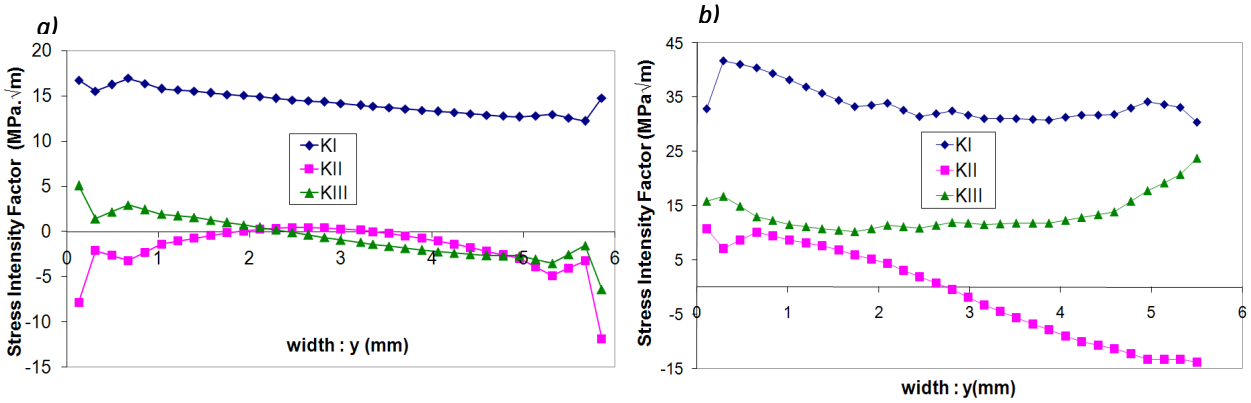

Figure 8: SIFs at peak load along the 7th crack fronts in a) Al specimen CCP5a b) steel specimen CCP2a.

The crack growth rates measured at various depths in these specimens are plotted versus ΔK_I on Fig. 9a and versus $\Delta K_{eq} = \sqrt{\Delta K_I^2 + \Delta K_{II}^2 + \frac{\Delta K_{III}^2}{(1-\nu)}}$ on Fig. 9b. While ΔK_I fails to correlate all the data, ΔK_{eq} provides a much better correlation, which gives additional evidence that opening and shear modes cooperate for slanted crack growth.

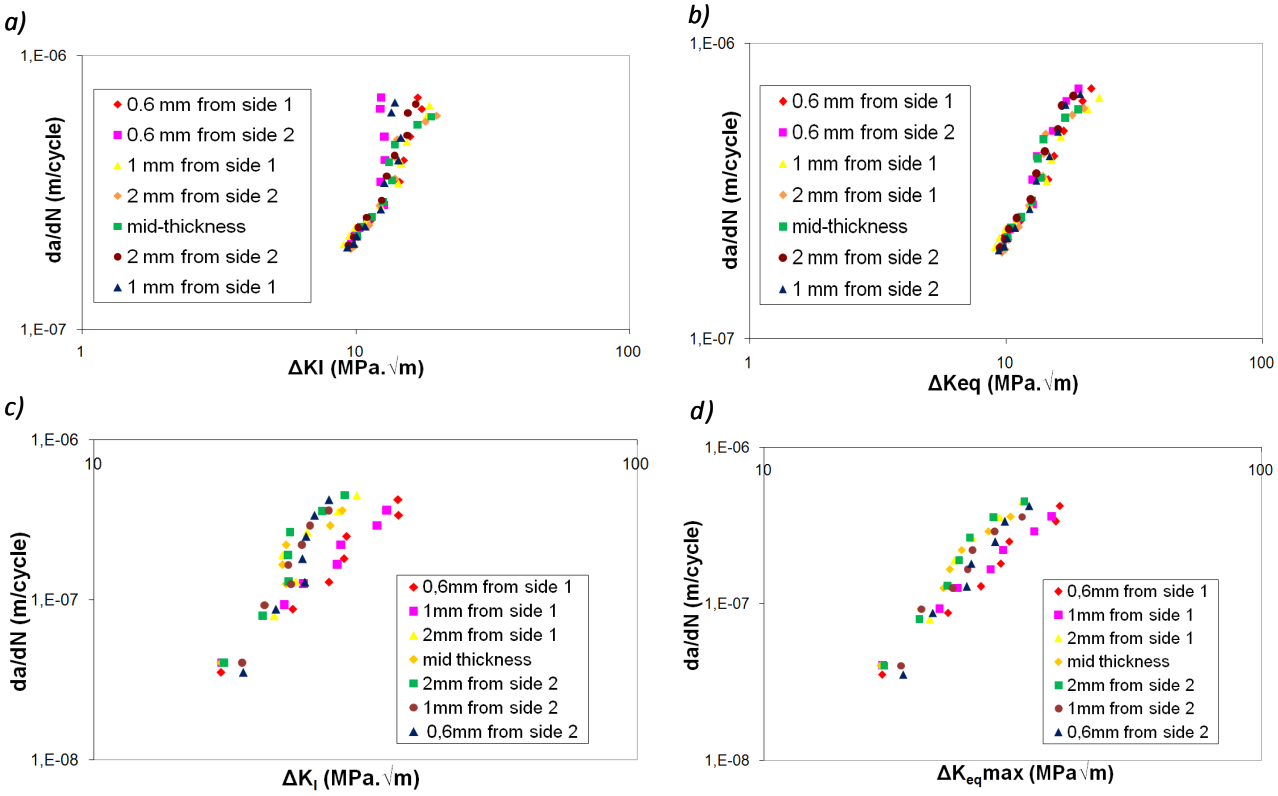

Figure 9: Correlation of measured crack growth rates in 7075-T6 with a) ΔK_I or b) ΔK_{eq} and in S355 steel with c) ΔK_I and d) ΔK_{eq}

5.2. Analysis of crack paths based on the local approach

Figure 10 shows the computed profiles of von Mises equivalent strain range ahead of the successive crack fronts for specimens CCP5a and CCP2a. Since ΔK increases as the crack grows, so does the equivalent strain range. $\Delta\varepsilon_{eq}$ rises near side surfaces. According to the fatigue criterion presented above, this should trigger a change in fracture mode (normal to slanted crack growth) there.

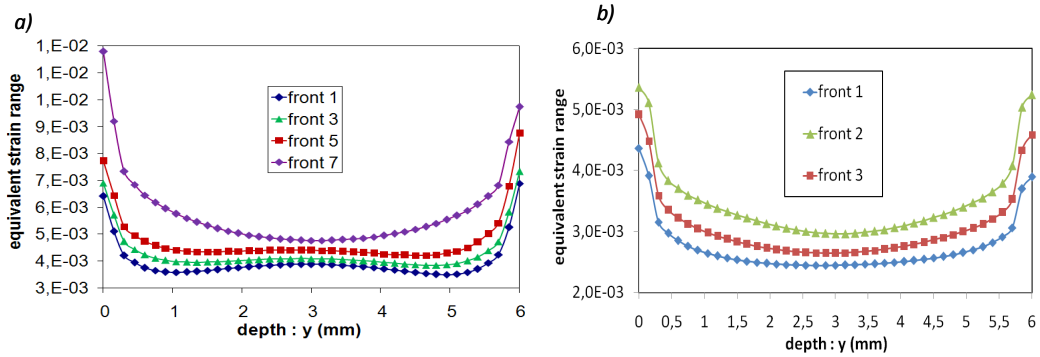

Figure 10: Profiles of Δ∈eq ahead of various crack fronts for a) specimen CCP5a and b) specimen CCP2a

Figure 11 shows the profiles of predicted twist angles. A progressive increase in twist angle as the crack grows is predicted near side surfaces. In some cases, as for the measured twist angles shown on Fig. 1b and 1d, the peak value of θ was not found at the free surface but somewhat inside.

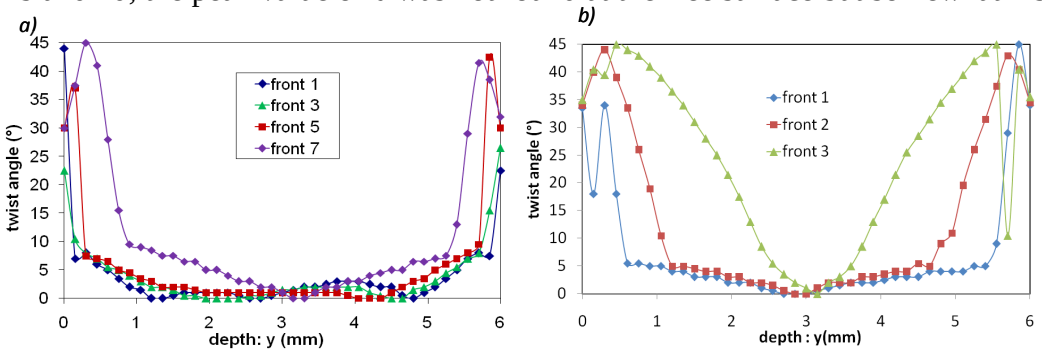

Figure 11: Profile of predicted twist angles for a) specimen CCP5a and b) specimen CCP2a

The shear lips width, t_s, was computed from such profiles, as the width of the part where $\theta \geq 4°$ in average. Figure 12 compares the predicted and measured evolutions of t_s. The model qualitatively captures the progressive increase in t_s.

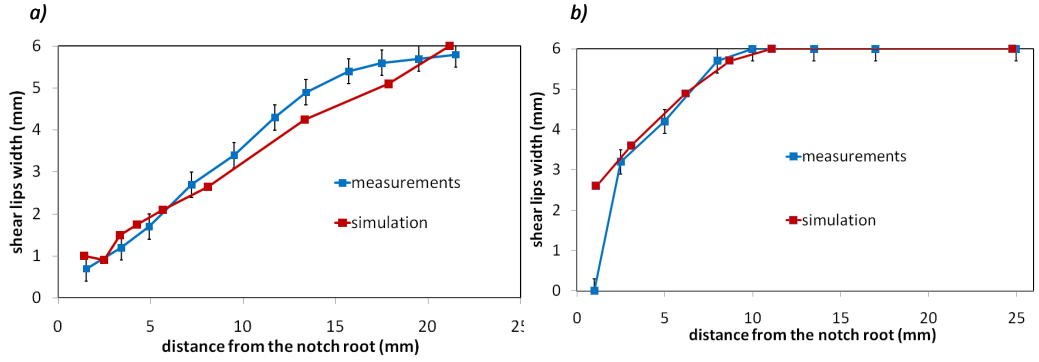

Figure 12: Predicted and measured evolution of shear lips width. a) ccp5a and b) ccp7a.

6. Conclusions and further work

Fatigue crack paths in thin sheets of aluminium alloy and mild steel were characterized in 3D in air and salt water. Crack twisting was delayed by a corrosive environment, which makes normal mode I crack growth more stable. Real 3D crack geometries were taken into account in an X-FEM model allowing the computation of K_I, K_{II}, K_{III} at any point along the front. Both the opening and shear modes contribute to slanted crack growth, whose rate correlates much better with $\Delta K_{eq} = \sqrt{\Delta K_I^2 + \Delta K_{II}^2 + \frac{\Delta K_{III}^2}{(1-\nu)}}$ than with ΔK_I. 3D elastic-plastic F.E. simulations and a local application of a fatigue criterion with a strain range-dependent critical plane qualitatively predicted the transition in crack growth mode and the twist angles. The challenge is now to develop incremental 3D simulations of mixed-mode slanted crack growth in a unified framework. The X-FEM method has to be modified to incorporate cyclic plasticity. This should allow predictions of both the crack growth kinetics and crack paths, based on the local approach mentioned above.

References

[1] J. Schijve, Shear lips on fatigue fractures in aluminium alloy sheet metal, *Eng. Fract. Mech*. 14 (1981), 789-800

[2] L.B. Vogelesang, J. Schijve, Environmental effects on fatigue fracture mode transitions observed in aluminium alloys, *Fat. Fract. Eng. Mat. & Struct*. 3 (1980) 85-98

[3] J. Zuidema, H.S. Blauw, Slant fatigue crack growth in Al 2024 sheet material, *Eng. Fract. Mech*. 29 (1988) 401-413

[4] J. Zuidema, M. Mannesse, Interaction of fatigue crack growth properties and crack surface geometry in Al 2024 , *Engng. Fract. Mechanics* 40 (1991) 105-117

[5] A.A. Shanyavsky, M.Z. Koronov, Shear lips on fatigue fractures of aluminium alloy sheets subjected to biaxial cyclic loads at various R-ratios, *Fat. Fract. Engng. Mat. Struct.* 17 (1994) 1003-1013

[6] S. Horibe, M. Nakamura, M. Sumita, The effect of seawater on fracture mode transition in fatigue, *Int. J. Fatigue* 7 (1985) 224-227

[7] K. Walker, S. Pendleberry, R. McElwee , Tensile and shear-mode cracking of titanium sheet in air and in salt water, in: *Effects of environment and complex load history on fatigue life*, p234-240, ASTM STP 462, ASTM Philadelphia (1970)

[8] L.P. Pook (1993), A finite element analysis of the angle crack specimen in*"Mixed-mode fracture and fatigue"* p 285-302, H.P. Rossmanith and K.J. Miller eds, ESIS 14, MEP, London

[9] A.Bakker, Three dimensional constraint effects on stress intensity distributions in plate geometries with through-thickness cracks, *Fat. Fract. Engng. Mat. Struct.*, 15 (1992) 1051-1069

[10] N. Moes, J. Dolbow and T. Belytschko, A finite element method for crack growth without remeshing *Int. Journ. Numerical Methods in Engineering* 46 (1999) 131-150

[11] Ph. Destuynder, M. Djaoua, S. Lescure, Quelques remarques sur la mécanique de la rupture elastique, *Journ. Mécanique Théorique & Appliquée* 2 (1983) 113-135

[12] T. Zhao, Y. Jiang Fatigue of 7075-T651 aluminum alloy *Int. J. Fatigue* 30 (2008) 834–849